Allosteric inhibition of *Acinetobacter baumannii* ATP phosphoribosyltransferase by protein:dipeptide and protein:protein interactions

Benjamin J. Read,[†] Gemma Fisher,[†] Oliver L. R. Wissett,[†] Teresa F. G. Machado,[§] John Nicholson,[†] John B. O. Mitchell,[§] and Rafael G. da Silva[†,*]

[†]School of Biology, Biomedical Sciences Research Complex, University of St Andrews, St Andrews, Fife KY16 9ST, United Kingdom

[§]School of Chemistry, Biomedical Sciences Research Complex, University of St Andrews, St Andrews, Fife KY16 9ST, United Kingdom

*To whom correspondence may be addressed: rgds@st-andrews.ac.uk, phone: +44 (0)1334 463496

Abstract. ATP phosphoribosyltransferase (ATPPRT) catalyses the first step of histidine biosynthesis in bacteria, namely the condensation of ATP and 5-phospho-α-D-ribosyl-1-pyrophosphate (PRPP) to generate N^1-(5-phospho-β-D-ribosyl)-ATP (PRATP) and pyrophosphate. Catalytic ($HisG_S$) and regulatory (HisZ) subunits assemble in a hetero-octamer where HisZ activates $HisG_S$ and mediates allosteric inhibition by histidine. In *Acinetobacter baumannnii*, $HisG_S$ is necessary for the bacterium to persist in the lung during pneumonia. Inhibition of ATPPRT is thus a promising strategy for specific antibiotic development. Here *A. baumannii* ATPPRT is shown to follow a rapid equilibrium random kinetic mechanism, unlike any other ATPPRT. Histidine noncompetitively inhibits ATPPRT. Binding kinetics indicates histidine binds to free ATPPRT and to ATPPRT:PRPP and ATPPRT:ATP binary complexes with similar affinity following a two-step binding mechanism, but with distinct kinetic partition of the initial enzyme:inhibitor complex. The dipeptide histidine-proline inhibits ATPPRT competitively and likely uncompetitively, respectively, against PRPP and ATP. Rapid kinetics analysis shows His-Pro binds to the ATPPRT:ATP complex via a two-step binding mechanism. A related HisZ that shares 43% sequence identity with *A. baumannii* HisZ is a tight-binding allosteric inhibitor of *A. baumannii* $HisG_S$. These findings lay the foundation for inhibitor design against *A. baumannii* ATPPRT.

Keywords: ATP phosphoribosyltransferase; enzyme inhibition; protein:protein interaction; *Acinetobacter baumannii*, kinetic mechanism

The dissemination of drug-resistant bacteria poses an alarming threat to global public health. The World Health Organisation recently published a list of 12 bacteria against which the development of novel drugs is of utmost priority, atop of which carbapenem-resistant *Acinetobacter baumannii* was placed.[1] *A. baumannii* is a Gram-negative bacterium responsible for ~2% of hospital-acquired infections in the United States[2] and between ~1% and ~30% in Europe, depending on the country.[3] Globally, ~44% of *A. baumannii* isolates are multidrug resistant, rising to 70% in the Middle East and Latin America.[4] One of most common manifestations of *A. baumannii* infection is ventilator-associated pneumonia.[5] Owing to the clinical and economic impact of infections by multidrug-resistant *A. baumannii*,[6] novel antibiotics are urgently needed to combat such infections, especially pneumonia,[7-8] and the characterisation of promising molecular targets and is a paramount step to underpin rational drug development.[9]

L-histidine metabolism offers an attractive opportunity for the development of novel antibiotics to treat pneumonia caused by *A. baumannii*. For instance, histidine catabolism is necessary for biofilm formation in *A. baumannii*, and urocanase-defective strains cannot form biofilms.[10] Histidine ammonia-lyase is an essential enzyme in *A. baumannii* for histidine-mediated zinc scavenging and mobilisation in host-imposed zinc starvation during pneumonia,[11] and for persistence of the bacterium in the lung during pneumonia.[8] While histidine is detected in the extracellular space in the lungs of mice, its concentration is lower than 2 μM independent of infection with *A. baumannii*.[8] Hence it is not surprising that high-throughput transposon library analysis demonstrated that six enzymes of the histidine biosynthetic pathway are necessary for *A. baumannii* persistence in the lung during pneumonia.[12] In agreement, individual knockout of the gene encoding the HisF subunit of the histidine biosynthetic enzyme imidazole glycerol phosphate synthase in *A. baumannii*

drastically increased host survival in mouse models of pneumonia.[7] The histidine biosynthesis pathway is absent in mammals, which bodes well for drug discovery vis-à-vis target specificity.

ATP phosphoribosyltransferase (ATPPRT) (EC 2.4.2.17) is one of the six histidine biosynthetic enzymes necessary for maintenance of *A. baumannii* bacterial load during pneumonia.[12] ATPPRT catalyses the first and flux-controlling step of histidine biosynthesis, the Mg^{2+}-dependent and reversible condensation of ATP and 5-phospho-α-D-ribosyl-1-pyrophosphate (PRPP) to generate N^1-(5-phospho-β-D-ribosyl)-ATP (PRATP) and pyrophosphate (PP_i). The reaction equilibrium is drastically displaced towards the reactants,[13] and enzyme activity is subjected to negative feedback control via allosteric inhibition by histidine (Scheme 1).[14-15]

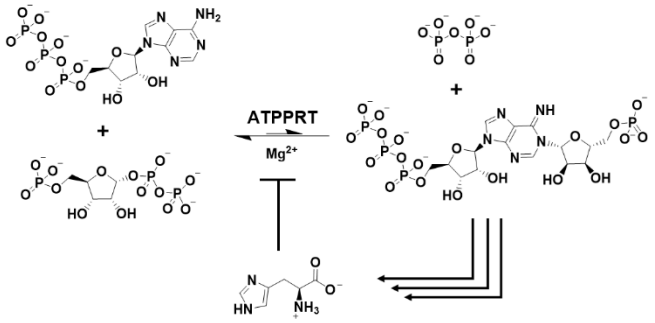

Scheme 1. ATPPRT-catalysed reaction is allosterically inhibited by L-histidine.

The *hisG* gene encodes two forms of ATPPRT, depending on the species. The long form of the protein, $HisG_L$, encompasses two N-terminal catalytic domains and a C-terminal allosteric domain, the latter mediating inhibition by histidine, arranged in a homohexamer.[16-17] The short form of the protein, $HisG_S$, comprises the two catalytic domains but lacks the C-terminal histidine-binding domain.[18] $HisG_S$ on its own is dimeric, displays low catalytic activity, and is insensitive to inhibition by histidine.[19-20] $HisG_S$ forms a hetero-octamer of 1:1 stoichiometry with the regulatory protein HisZ, a paralogue of histidyl-tRNA synthetase with no catalytic ability of its own.[18, 21-22] HisZ allosterically activates $HisG_S$ catalysis and harbours

the histidine binding site to mediate allosteric inhibition by the final product of the biosynthetic pathway.[19-20, 23-24] *A. baumannii* possesses the short-form ATPPRT, and while the HisG$_S$-encoding gene is necessary for this pathogen's persistence in the lung during pneumonia, intriguingly the HisZ-encoding gene is essential for *A. baumannii* growth in rich medium.[12]

In this work, constructs encoding *A. baumannii* HisG$_S$ (*Ab*HisG$_S$) and HisZ (*Ab*HisZ) were cloned and expressed, the recombinant proteins were individually purified, and the hetero-octameric holoenzyme (*Ab*ATPPRT) reconstituted *in vitro*. Initial velocity patterns in the absence and presence of product and dead-end inhibitors suggest a unique kinetic mechanism among ATPPRTs. Inhibition by histidine and histidine-proline (His-Pro) dipeptide are characterised by steady-state kinetics and fluorescence-based binding kinetics. Finally, tight-binding inhibition of *Ab*HisG$_S$ by an orthologous HisZ is reported. This may pave the way for future drug discovery targeting *Ab*ATPPRT.

RESULTS AND DISCUSSION

Purification and biophysical characterisation of *Ab*ATPPRT. *Ab*HisG$_S$ and *Ab*HisZ were purified to homogeneity as estimated by Coomassie Blue-stained SDS-PAGE (Figure S1A). Electrospray-ionisation mass spectrometry (ESI-MS) analysis resulted in molecular mass of 25137.2 and 42917.6 for *Ab*HisG$_S$ and *Ab*HisZ (Figure S1B,C), respectively, exactly matching the predicted theoretical values based on the amino acid sequence of each protein, which contains a Gly residue at the N-terminus as a result of cleavage with tobacco etch virus protease (TEVP).

Analytical size-exclusion chromatography (Figure S2) indicated *Ab*ATPPRT has a mass of ~240000, which is somewhat lower than the expected mass for a hetero-octameric quaternary structure of four *Ab*HisG$_S$ and four *Ab*HisZ subunits (~271000). This is possibly caused by the relatively lower resolution of the technique near that mass range. We used the

well-characterised *Psychrobacter arcticus* $HisG_S$, which is strictly dimeric *in crystallo* and in solution,[25] as a control in the size-exclusion chromatography, and obtained a mass of ~47000, in good agreement with the predicted mass for the dimer (~50000). Surprisingly, *Ab*$HisG_S$ analysis yielded a mass of ~30000, which is consistent with a monomeric quaternary structure, even though *Ab*$HisG_S$ and *P. arcticus* $HisG_S$ share 69% amino acid sequence identity.[25]

Differential scanning fluorescence (DSF)-based thermal denaturation analysis (Figure S3A,B) showed both PRPP and ATP can bind to *Ab*$HisG_S$ leading to an increase in the protein melting temperature (T_m) (Table S1). This is in contrast to results reported for *P. arcticus* $HisG_S$ where only PRPP could bind to the protein.[26] DSF analysis suggests that histidine cannot bind to free *Ab*HisZ (Figure S3C), as the T_m is unchanged upon increasing histidine concentration (Table S1).

Allosteric activation and kinetic mechanism of *Ab*ATPPRT. *Ab*$HisG_S$ is catalytically active and insensitive to the presence of histidine in the absence of *Ab*HisZ (Figure 1A). This conforms with previous reports of residual catalytic activity by $HisG_S$ in the absence of HisZ.[19-20] *Ab*$HisG_S$ substrate saturation curves displayed Michaelis-Menten kinetics when either PRPP or ATP concentration was varied (Figure S4), and fit to eq 1 yielded apparent steady-state catalytic rate constant (k_{cat}) equal to 0.12 ± 0.05 s^{-1} and apparent Michaelis constant (K_M) of 0.6 ± 0.1 mM and 0.63 ± 0.09 mM for PRPP (K_M^{PRPP}) and ATP (K_M^{ATP}), respectively. For comparison, Table S2 compiles steady-state kinetic parameters from this work and from the literature for several ATPPRTs. Even though the regulatory protein has no catalytic activity on its own, the presence of *Ab*HisZ to form *Ab*ATPPRT leads to a significant increase in reaction rate. In addition, it renders the holoenzyme sensitive to inhibition by histidine (Figure 1A). Increasing the concentration of *Ab*HisZ saturates *Ab*$HisG_S$ (Figure 1B), and data fitting to eq 2 resulted in an apparent equilibrium dissociation constant (K_D^{app}) of 40 ± 10 nM, which is used to calculate *Ab*ATPPRT concentration at any ratio of *Ab*HisZ to *Ab*$HisG_S$ via eq 3.

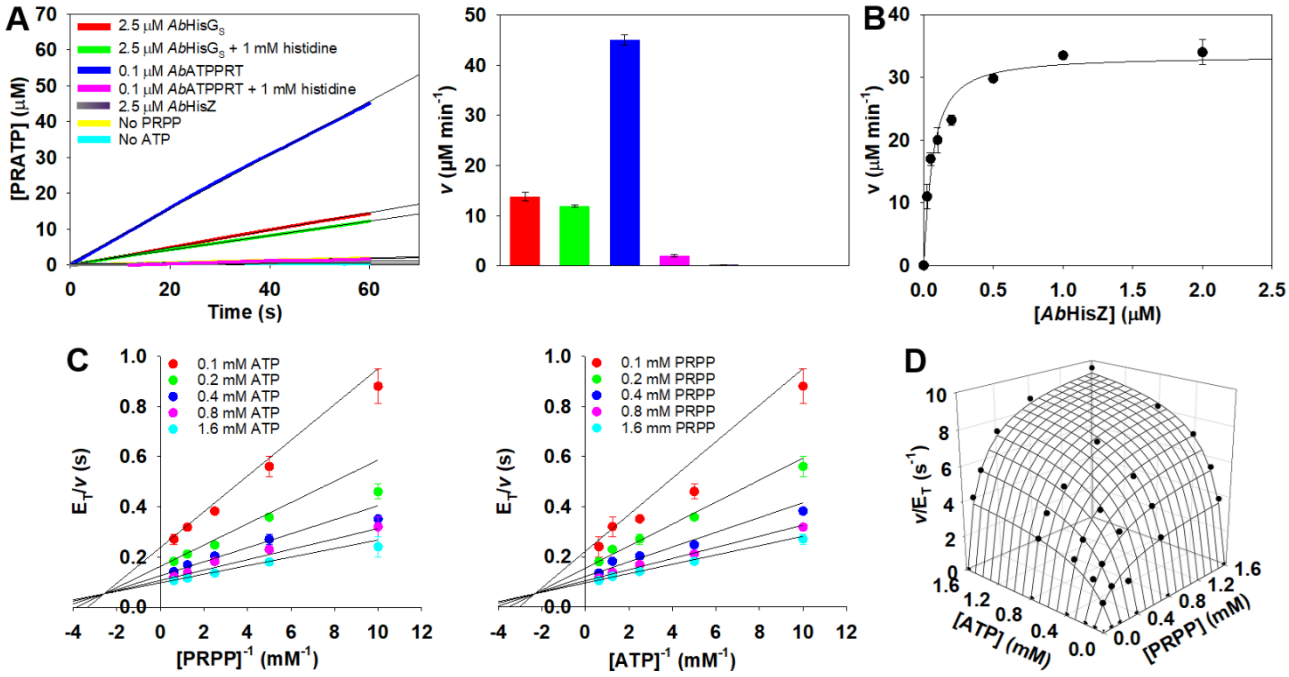

Figure 1. Allosteric control and kinetic mechanism of *Ab*ATPPRT. **(A)** Time course of product formation and bar-graph representation of the respective rates by *Ab*HisG$_S$ and *Ab*ATPPRT in the presence and absence of histidine. **(B)** *Ab*HisZ-dependent increase in reaction rate by *Ab*HisG$_S$. Line represents best fit to eq 2. **(C)** Double-reciprocal plots of *Ab*ATPPRT substrate saturation curves at varying concentrations of one substrate and different fixed concentrations of the other. **(D)** Three-dimensional plot of the initial rate data. Line represents best fit to eq 4.

HisG$_L$-type ATPPRTs follow a steady-state ordered mechanism where ATP must bind to the free enzyme, whereas binding of PRPP to the free enzyme leads to a dead-end binary complex.[27-28] Conversely, the HisG$_S$-type ATPPRT from *P. arcticus* follows a steady-state ordered mechanism where only PRPP is able to bind to the free enzyme, followed by ATP binding to the binary complex.[25-26] The indication that both PRPP and ATP can bind to *Ab*HisG$_S$ raised the possibility that *Ab*ATPPRT follows a different kinetic mechanism than those previously reported for both forms of ATPPRTs. Since knowledge of the kinetic mechanism can aid inhibitor design and the interpretation of inhibition mechanisms,[9, 29] the kinetic mechanism of *Ab*ATPPRT was investigated. Initial velocity patterns for *Ab*ATPPRT-

catalysed formation of PRATP (Figure 1C) intersect on the left of the *y*-axis, indicating the reaction proceeds by a sequential mechanism and ruling out a rapid equilibrium ordered kinetic mechanism. Global fit of the data to eq 4 (Figure 1D), which describes both rapid equilibrium random and steady-state ordered mechanisms, yielded k_{cat} of 11.4 ± 0.4 s^{-1}, K_M^{PRPP} of 0.15 ± 0.02, mM K_M^{ATP} of 0.17 ± 0.02 mM, and K_{ia} of 0.40 ± 0.01 mM regardless of which substrate was defined as substrate A. Remarkably, formation of the *Ab*ATPPRT holoenzyme leads to a 95-fold activation of catalysis relative to *Ab*HisG$_S$. For comparison, formation of the holoenzyme results in 4-fold activation of *P. arcticus* HisG$_S$[20] and 10-fold activation of *L. lactis* HisG$_S$.[19]

The order of substrate binding to an enzyme can be gleaned from the mode of inhibition of that enzyme by reaction products and/or dead-end inhibitors.[30] PRATP is a competitive inhibitor of *Ab*ATPPRT against both PRPP and ATP at low (~K_M) and high (~10K_M) fixed concentrations of the co-substrate (Figure 2A,B), and data fit to eq 5 yielded slope inhibition constants (K_{is}) summarised in Table S3. In all cases, the K_{is} increases as the concentration of the co-substrate increases, which is characteristic of rapid equilibrium random systems.[31] Owing to the necessity to use a pyrophosphatase (PPase) in the activity assay to displace the unfavourable equilibrium towards the forward reaction,[20] PP_i could not be used in product inhibition. Instead, the PP_i analogue phosphonoacetate (POAc), was employed as a dead-end inhibitor. POAc is a very slow substrate that replaces PP_i in the reverse reaction of some ATPPRTs.[32] When POAc was tested as a substrate replacing PP_i in the *Ab*ATPPRT reverse reaction under the same conditions and timeframe of the inhibition studies, the rate constant for PRATP consumption was less than 0.1% of that observed with PP_i (Figure S5), thus POAc was treated as an inhibitor. POAc is a competitive inhibitor of *Ab*ATPPRT against ATP at both low (~K_M) and high (~10K_M) fixed concentrations of PRPP (Figure 2C), and a noncompetitive inhibitor of the enzyme against PRPP at low (~K_M) fixed concentrations of ATP (Figure 2D).

K_{is} and intercept inhibition constant (K_{ii}) values obtained upon data fitting to either eq 5 or eq 6 are shown in Table S3. However, when the fixed ATP concentration is high (~10K_M), POAc inhibition of *Ab*ATPPRT against PRPP is drastically weakened, and a partial dose-responsive curve can only estimate that the half-maximal inhibitory concentration (IC_{50}) is higher than 10 mM, since at this concentration more than 60% of *Ab*ATPPRT activity remains (Figure 2E).

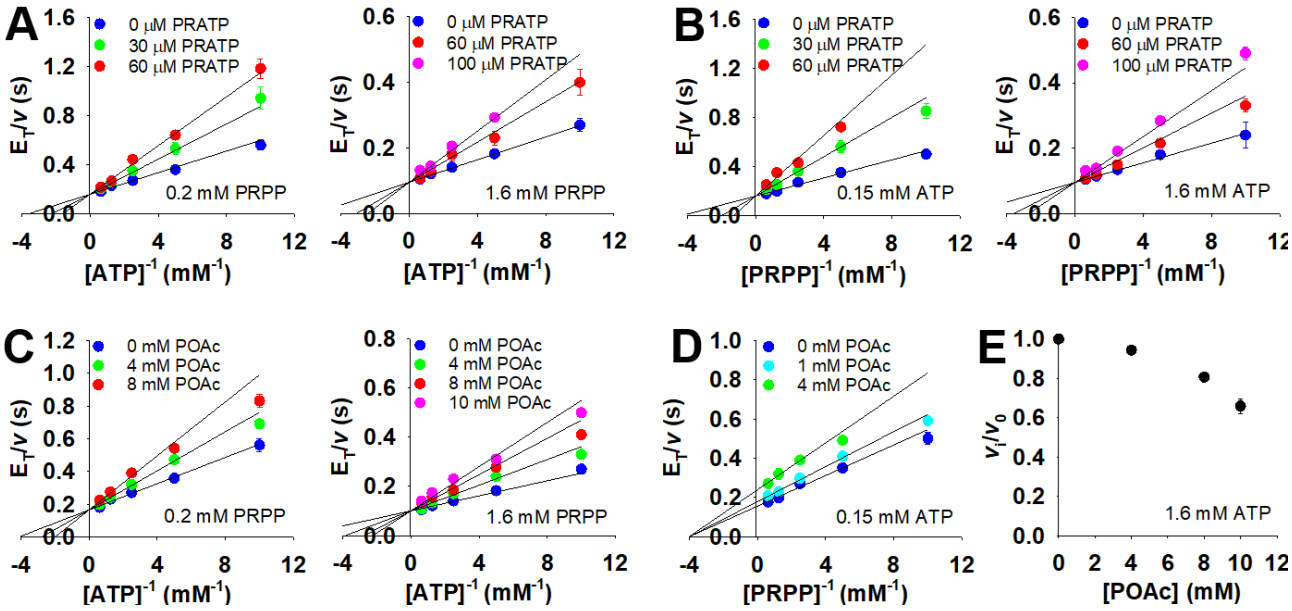

Figure 2. Product and dead-end inhibition of *Ab*ATPPRT. **(A)** Double-reciprocal plots of *Ab*ATPPRT ATP saturation curves in the presence of PRATP at sub-saturating and saturating PRPP. **(B)** Double-reciprocal plots of *Ab*ATPPRT PRPP saturation curves in the presence of PRATP at sub-saturating and saturating ATP. **(C)** Double-reciprocal plots of *Ab*ATPPRT ATP saturation curves in the presence of POAc at sub-saturating and saturating PRPP. **(D)** Double-reciprocal plots of *Ab*ATPPRT PRPP saturation curves in the presence of POAc at sub-saturating ATP. **(E)** Partial dose-response curve for *Ab*ATPPRT against POAc at saturating ATP and 0.8 mM PRPP. Lines are reciprocals of the best fit of the data to either eq 5 (**A – C**) or eq 6 (**D**).

This pattern of product and dead-end inhibition is uniquely consistent with a rapid-equilibrium random kinetic mechanism[31] for *Ab*ATPPRT, with both PRPP and ATP capable to

bind to the free enzyme to form productive binary complexes. DSF analysis showed *Ab*HisG$_S$ T_m increases in the presence of PRATP, but not of PP$_i$ (Figure S6A). Importantly, the presence of PRATP also increases the T_m of *Ab*ATPPRT, while the presence of PP$_i$ does not (Figure S6B). While the possibility exists that PP$_i$ binds to free *Ab*HisG$_S$ and free *Ab*ATPPRT without affecting its T_m, this observation suggests product release from the enzyme is ordered or with a strongly preferred order where PRATP departs last, as reported for both HisG$_L$- and HisG$_S$-type ATPPRTs.[26-27] The proposed kinetic mechanism for *Ab*ATPPRT with a rapid equilibrium random addition of substrates and an ordered dissociation of products is shown in Scheme S1.

Histidine is a noncompetitive inhibitor of *Ab*ATPPRT. Histidine inhibits *Ab*ATPPRT with an IC$_{50}$ of 135 ± 3 μM and a Hill coefficient (h) of 1.52 ± 0.05 (Figure 3A). This IC$_{50}$ is ~4-fold higher than those for *Mycobaterium tuberculosis* ATPPRT (IC$_{50}$ = 33 μM, h = 1.5)[33] and *P. arcticus* ATPPRT (IC$_{50}$ = 35 μM, h = 1.3).[24] Inhibition is mixed-type noncompetitive against PRPP and noncompetitive against ATP (Figure 3B), and best fit of the data to eq 6 yielded apparent K_{is} (K_{is}^{app}) and K_{ii}^{app} of 83 ± 16 μM and 245 ± 36 μM, respectively, against PRPP, and K_{is}^{app} = K_{ii}^{app} of 282 ± 31 μM against ATP. Except for *M. tuberculosis* ATPPRT, where inhibition is uncompetitive against ATP,[33] histidine is a noncompetitive inhibitor of other ATPPRTs.[15-16, 22, 34]

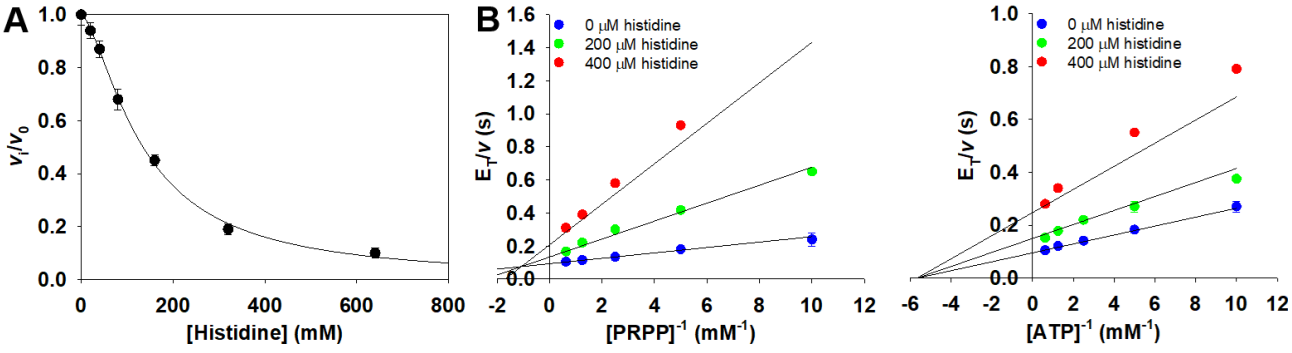

Figure 3. Inhibition of *Ab*ATPPRT by histidine. **(A)** Dose-response curve for histidine. The line is best fit of the data to eq 7. **(B)** Double-reciprocal plots of substrate saturation curves in the presence of histidine. Lines are reciprocals of the best fit of the data to eq 6.

Two-step binding mechanism of histidine to *Ab*ATPPRT. To gain detailed information on the interaction between *Ab*ATPPRT and histidine, the binding kinetics of the allosteric inhibitor to the different enzyme complexes was investigated following an overall increase in tryptophan fluorescence (all 3 tryptophan residues in *Ab*ATPPRT are found in *Ab*HisZ) upon histidine binding to either *Ab*ATPPRT, *Ab*ATPPRT:ATP binary complex, or *Ab*ATPPRT:PRPP binary complex (Figure 4). Three models were tested to fit the data by numerical integration using KinTek Explorer[35]: one-step binding, two-step binding with isomerisation of the enzyme:inhibitor complex, and two-step binding with isomerisation of the free enzyme prior to binding (Scheme S2), without any assumptions regarding rate-limiting steps. For each data set, only the two-step binding mechanism with isomerisation of the initial enzyme:inhibitor complex converged on a solution, and FitSpace confidence contour analysis[36] confirmed the model was well constrained. Table 1 summarises the calculated rate constants.

Table 1. Rate constants governing histidine binding to *Ab*ATPPRT.[a]

Enzyme	k_1 (M^{-1} s^{-1})	k_2 (s^{-1})	k_3 (s^{-1})	k_4 (s^{-1})
***Ab*ATPPRT**	$(2.75 \pm 0.0009) \times 10^4$ *$(2.55\text{-}9.27) \times 10^4$*	10.2 ± 0.1 *(7.7-13.9)*	12.0 ± 0.1 *(9.4-15.9)*	1.87 ± 0.04 *(1.11-2.92)*
***Ab*ATPPRT: ATP**	$(3.88 \pm 0.007) \times 10^4$ *$(3.31\text{-}4.37) \times 10^4$*	5.2 ± 0.2 *(3.3-6.9)*	5.1 ± 0.2 *(3.3-9.4)*	1.25 ± 0.04 *(0.74-1.98)*
***Ab*ATPPRT: PRPP**	$(5.1 \pm 0.002) \times 10^3$ *$(4.9\text{-}6.0) \times 10^3$*	1.20 ± 0.07 *(0.50-1.77)*	6.9 ± 0.3 *(5.8-9.1)*	1.75 ± 0.03 *(1.47-2.68)*

[a]Values in normal text represent mean ± best fit uncertainty from the numerical integration, while values in italics represent FitSpace lower and upper boundaries.

While histidine binding to *Ab*ATPPRT in its apo form and in binary complexes with ATP and PRPP involves the same overall two-step mechanism, kinetic differences exist among specific steps. The ratio of forward-to-reverse rate constants for breakdown of the intermediate (k_3/k_2) is ~1 when the intermediate is either *Ab*ATPPRT:histidine or *Ab*ATPPRT:ATP:histidine, and increases to 5.8 for *Ab*ATPPRT:PRPP:histidine, thus a rapid equilibrium between inhibitor-free enzyme and intermediate is not established. The bimolecular rate constant (k_1) is approximately one order of magnitude lower when histidine binds to *Ab*ATPPRT:PRPP in comparison to binding to *Ab*ATPPRT and *Ab*ATPPRT:ATP, but in all cases k_3 is significantly higher than k_4, leading to accumulation of the isomerised complexes as illustrated by simulations of the time-dependent changes in concentration of each *Ab*ATPPRT species carried out in KinTek Explorer (Figure S7 – S9). Eq 8 was used to calculate overall K_D of 50 ± 1 μM, 26 ± 1 μM, and 48 ± 3 μM for the dissociation of histidine from *Ab*ATPPRT:histidine, *Ab*ATPPRT:ATP:histidine and *Ab*ATPPRT:PRPP:histidine complexes, respectively, indicating the presence of either substrate in turn has little influence on the overall affinity of the enzyme (or its binary complex with each substrate) for histidine, in spite of differences in individual rate constants for elementary steps. It should not be surprising that inhibition by histidine involves two steps, since it is known to be allosteric. Nonetheless, the results establish a sequential mechanism of ligand-binding,[37] and demonstrate that the common assumption of a rapid equilibrium between the initial free and bound states followed by a slower isomerisation of the bound state, invoked to obtain an analytical solution to the differential equation describing the process,[38-39] does not hold true for the *Ab*ATPPRT:histidine interaction.

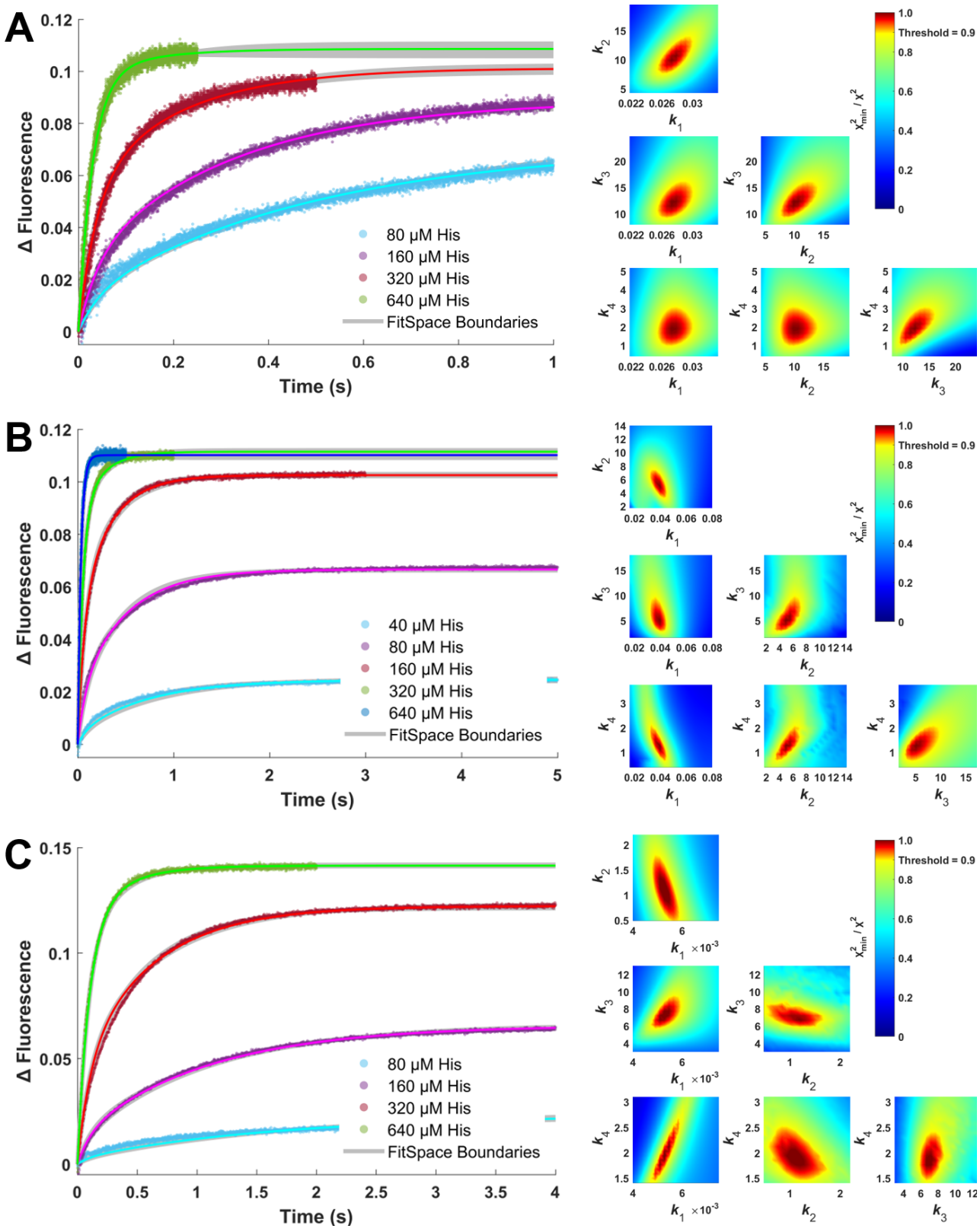

Figure 4. Binding kinetics of histidine to *Ab*ATPPRT. **(A)** Histidine binding to *Ab*ATPPRT. **(B)** Histidine binding to *Ab*ATPPRT:ATP. **(C)** Histidine binding to *Ab*ATPPRT:PRPP. For curves (panels on the left), scatter plots represent data, coloured lines are numerical integration-

based best fit of the data to a two-step model with isomerisation of the enzyme:inhibitor complex, and grey lines are the boundaries produced by FitSpace analysis. The contour plots (panels on the right) are FitSpace analysis of the best-fit model relative to the data. The constrained FitSpace boundaries are defined by the regions in red. Notice k_1 has units of μM^{-1} s^{-1} in the contour plots.

His-Pro dipeptide is an inhibitor *Ab*ATPPRT. As an attempt to identify potential allosteric inhibitors of *Ab*ATPPRT, 12 commercially available histidine analogues (Chart S1) were screened as potential inhibitors of the enzyme. None of the compounds inhibited *Ab*ATPPRT at a single compound concentration of 2 mM, although 3 compounds seemed to enhance enzyme activity (Figure S10A). However, further dose-response curves for these 3 compounds revealed no effect on *Ab*ATPPRT activity (Figure S10B).

To expand the search for inhibitors of *Ab*ATPPRT, 14 readily available dipeptides containing a histidine residue either on the N-terminus or C-terminus (Chart S2) were screened at a single concentration of 1 mM (except for His-Trp, whose concentration was 0.25 mM) against the enzyme. His-Trp and His-Pro decreased *Ab*ATPPRT activity by a minimum of 30% (Figure S11). Dose-response of His-Trp showed a consistent inhibition trend, but a maximum of only 45% inhibition was experimentally achieved since His-Trp concentrations higher than 0.4 mM interfered with the assay owing to indole absorbance at 290 nm (Figure 5A). His-Pro inhibits *Ab*ATPPRT with an IC_{50} of 1.6 ± 0.1 mM and an h of 1.28 ± 0.09 (Figure 5A). Unlike histidine, His-Pro inhibits *Ab*ATPPRT competitively against PRPP (Figure 5B), and best fit of the data to eq 5 yielded a K_{is}^{app} of 1.1 ± 0.3 mM. Based on data fit quality, inhibition against ATP could be interpreted as either noncompetitive (Figure 5C), yielding $K_{is}^{app} = K_{ii}^{app}$ of 5.5 ± 0.4 mM upon best fit of the data to eq 6, or uncompetitive (Figure 5D), yielding K_{ii}^{app} of 4.2 ± 0.4 mM upon best fit of the data to eq 9. Thus, further evidence is needed to distinguish between the two models.

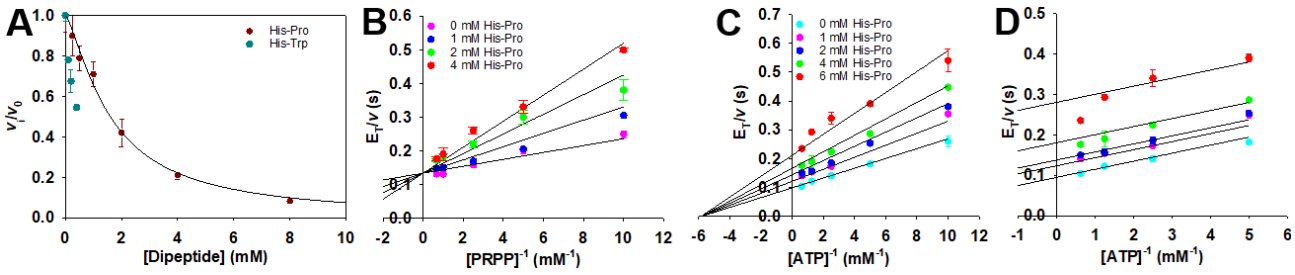

Figure 5. Inhibition of *Ab*ATPPRT by His-Pro. **(A)** Dose-response curve for His-Pro and His-Trp. The line is best fit of the data to eq 7. **(B)** Double-reciprocal plots of PRPP saturation curves in the presence of His-Pro. Lines are reciprocals of the best fit of the data to eq 5. **(C)** Double-reciprocal plots of ATP saturation curves in the presence of His-Pro. Lines are reciprocals of the best fit of the data to eq 6. **(D)** Double-reciprocal plots of ATP saturation curves in the presence of His-Pro. Lines are reciprocals of the best fit of the data to eq 9. The colour scheme is the same in panels C and D.

*Ab*HisG$_S$ dose-response curve for His-Pro reaches a plateau with ~70% of enzyme activity remaining (Figure S12A). This might suggest partial inhibition of the nonactivated enzyme by His-Pro. However, DSF analysis showed the *Ab*HisG$_S$ T_m is unaltered in the presence of His-Pro (Figure S12A, inset). This suggests the presence of *Ab*HisZ is necessary for full inhibition, and that the apparent effect of His-Pro on *Ab*HisG$_S$ is due to non-specific binding. A hypothesis for the mode of inhibition by His-Pro is that the dipeptide acts by dissociating the hetero-octamer or somehow disrupting the allosteric activation of *Ab*HisG$_S$ by *Ab*HisZ. In this case, the His-Pro-inhibited rate of *Ab*ATPPRT would be equal to the His-Pro-(partially)-inhibited rate of non-activated *Ab*HisG$_S$. This hypothesis was tested by measuring the reaction rates of 6 µM *Ab*HisG$_S$ in the absence and presence of His-Pro to compare with the rate of 6 µM *Ab*ATPPRT (containing 6 µM *Ab*HisG$_S$ saturated with *Ab*HisZ) in the presence His-Pro (Figure S12B). The rate of *Ab*ATPPRT in the presence of His-Pro is significantly lower than the rate *Ab*HisG$_S$ in the presence of His-Pro, suggesting that inhibition of *Ab*ATPPRT by the dipeptide is not achieved by simply preventing allosteric activation of the catalytic subunit.

The cyclic version of the dipeptide, cyclo-di-His-Pro, was also tested as an inhibitor of *Ab*ATPPRT, but no inhibition was detected (Figure S13), indicating the linear scaffold of the dipeptide is required for inhibition.

Two-step binding mechanism of His-Pro to *Ab*ATPPRT. To gather further insight into the interaction between *Ab*ATPPRT and His-Pro, the binding kinetics of the dipeptide to the enzyme was investigated following an overall increase in tryptophan fluorescence upon His-Pro binding (Figure S14). While the increase in fluorescence was consistent with formation of an *Ab*ATPPRT:His-Pro complex, the apparent change in signal amplitude did not indicate saturation of the enzyme up to 8 mM His-Pro, indicating very low affinity. However, binding of His-Pro to *Ab*ATPPRT:ATP complex occurred with faster kinetics and led to saturation (Figure 6). This is consistent with His-Pro in the experimental concentration range uncompetitively inhibiting *Ab*ATPPRT against ATP.

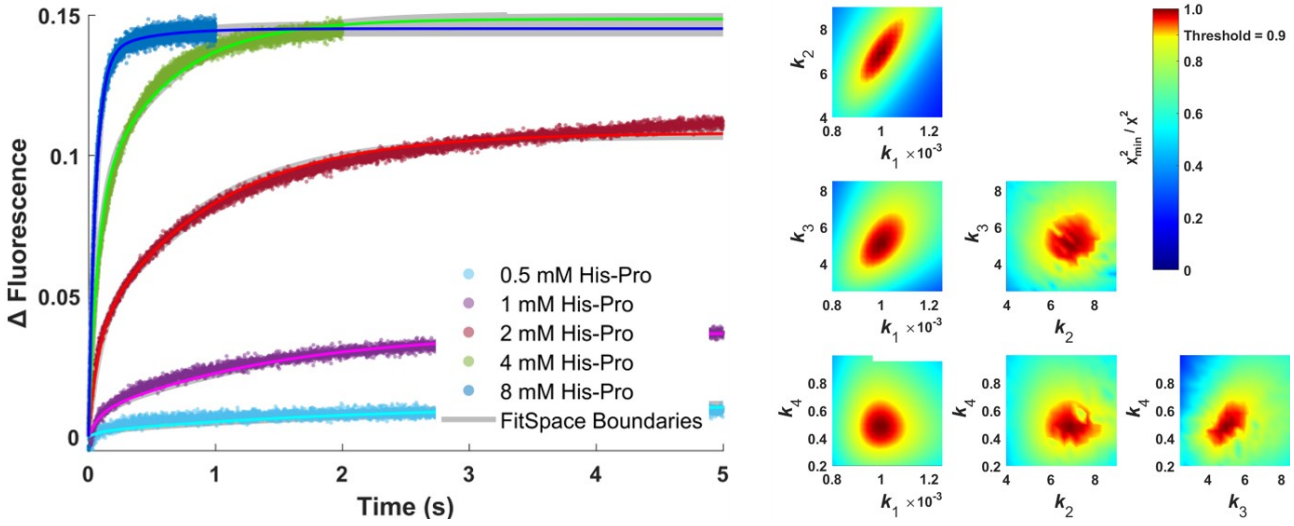

Figure 6. Binding kinetics of His-Pro to *Ab*ATPPRT:ATP. For curves (left), scatter plots represent data, coloured lines are numerical integration-based best fit of the data to a two-step model with isomerisation of the enzyme:inhibitor complex, and grey lines are the boundaries produced by FitSpace analysis. The contour plots (right) are FitSpace analysis of the best-fit

model relative to the data. The constrained FitSpace boundaries are defined by the regions in red. Notice k_1 has units of μM^{-1} s^{-1} in the contour plots.

The only model that converged to a solution by numerical integration was a two-step model involving an isomerisation of the initial enzyme:inhibitor complex, producing the following rate constants: k_1 = 1003 ± 6 M^{-1} s^{-1}; k_2 = 6.94 ± 0.03 s^{-1}; k_3 = 5.05 ± 0.05 s^{-1}; k_4 = 0.476 ± 0.006 s^{-1}. The model is well-constrained as indicated by FitSpace analysis (Figure 6), which yielded the following boundaries: k_1 = 920-1090 M^{-1} s^{-1}; k_2 = 5.58-8.47 s^{-1}; k_3 = 4.08-6.61 s^{-1}; k_4 = 0.326-0.663 s^{-1}. The ratio k_3/k_2 is only ~0.72, thus the possibility that His-Pro is a slow-onset inhibitor was considered, but no curvature was observed in *Ab*ATPPRT progress curves at various concentrations of dipeptide (Figure S15). The reverse isomerisation rate constant k_4 is more than 10-fold lower than k_3, leading to accumulation of the isomerised complex as illustrated by simulations of the time-dependent changes in concentration of each *Ab*ATPPRT species performed in KinTek Explorer (Figure S16). Eq 8 yielded an overall K_D of 0.60 ± 0.01 mM for inhibitor dissociation from the *Ab*ATPPRT:ATP:His-Pro complex. As in the case of histidine binding, here k_2 is not significantly higher than k_3, thus a rapid equilibrium is not established between initial free and bound states isomerisation.

***P. arcticus* HisZ is a tight-binding inhibitor of *Ab*HisG$_S$.** *A. baumannii* and *P. arcticus* belong to the same bacterial family, Moraxellaceae, and *Ab*HisG$_S$ and *Ab*HisZ share 69% and 43% amino acid sequence identity with their respective orthologues in *P. arcticus* (Figure S17). Given the similarity between the proteins, the hypothesis that *P. arcticus* HisZ would bind to and activate catalysis by *Ab*HisG$_S$ was evaluated. Surprisingly, *P. arcticus* HisZ is an inhibitor of *Ab*HisG$_S$ catalysis (Figure 7A), and best fit of the data to eq 10 produced a K_i^{app} of 0.34 ± 0.04 μM. The analytical size-exclusion elution profile of an equimolar *P. arcticus* HisZ/*Ab*HisG$_S$ mixture overlaps with that of the *Ab*HisZ/*Ab*HisG$_S$ mixture (Figure S2), raising the possibility the hybrid *P. arcticus* HisZ:*Ab*HisG$_S$ complex adopts a similar

oligomeric state in solution as *Ab*ATPPRT does. Nonetheless, current data do not permit a definitive conclusion to be reached, and further analysis employing higher resolution techniques will be necessary to dissect the oligomeric state and stoichiometry of the *P. arcticus* HisZ:*Ab*HisG$_S$ interaction. As a control for the specificity of the interspecies protein-protein interactions presumably causing inhibition of *Ab*HisG$_S$, the effect of bovine serum albumin on the *Ab*HisG$_S$ reaction was assessed, but it was not detected (Figure S18). *Ab*HisG$_S$ inhibition by *P. arcticus* HisZ was repeated in the presence of 600 µM histidine, but it did not lead to any significant difference in K_i^{app} (Figure S19A).

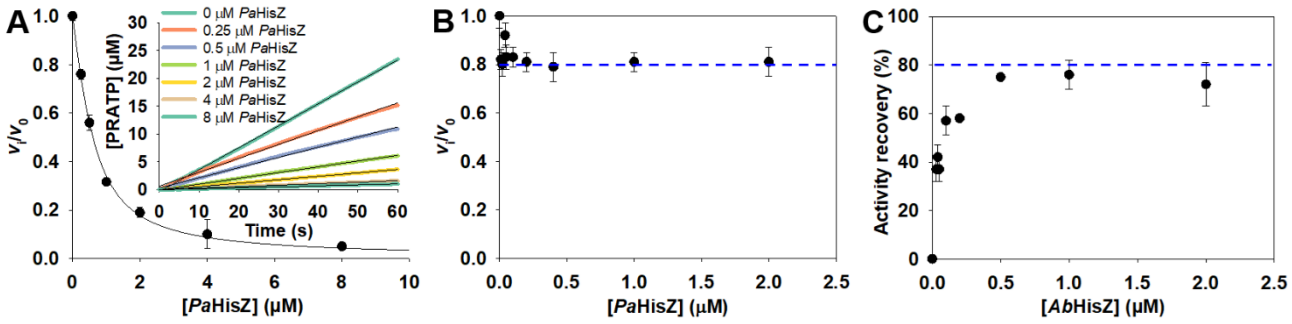

Figure 7. Inhibition of *Ab*HisG$_S$ by *P. arcticus* HisZ. *Pa* stands for *P. arcticus*. **(A)** Dose-response curve for *P. arcticus* HisZ against *Ab*HisG$_S$. The line is the best fit of the data to eq 10. The inset shows PRATP formation time course at increasing *P. arcticus* HisZ concentration, and black lines are linear regressions of the data. **(B)** Dose-response curve for *P. arcticus* HisZ against *Ab*ATPPRT. The dashed line demarks 80% of *Ab*ATPPRT uninhibited activity. **(C)** Dose-response of relative activity recovery of the *P. arcticus* HisZ:*Ab*HisG$_S$ complex upon increasing *Ab*HisZ concentration. The dashed line demarks 80% of *Ab*ATPPRT uninhibited activity.

P. arcticus HisZ seems to bind tightly to *Ab*ATPPRT as well, but once partial inhibition of *Ab*ATPPRT of ~20% is reached, further increases in *P. arcticus* HisZ have no effect on *Ab*ATPPRT catalysis (Figure 7B). This observation suggests a model of partial noncompetitive inhibition[31] against *Ab*HisZ, where *P. arcticus* HisZ can bind to *Ab*ATPPRT to form a *P.*

arcticus HisZ:*Ab*ATPPRT complex of unknown stoichiometry that can still generate product albeit at a lower rate than *Ab*ATPPRT, but can bind to *Ab*HisG$_S$ to form a fully inhibited complex. This model is further supported by the observation that a preformed inhibited complex of *P. arcticus* HisZ:*Ab*HisG$_S$ titrated with *Ab*HisZ recovers only ~80% of the activity of uninhibited *Ab*ATPPRT (Figure 7C), indicting even high *Ab*HisZ concentrations cannot completely overcome inhibition by *P. arcticus* HisZ. *Ab*ATPPRT inhibition by histidine was repeated in the presence of 2 μM *P. arcticus* HisZ, but no significant effect on the IC_{50} was observed (Figure S19B). However, a change in h from 1.4 ± 0.1 to 2.0 ± 0.1 suggests *P. arcticus* HisZ leads to an increase in the degree of positive co-operativity in inhibition by histidine, but the molecular basis for this phenomenon will require further research to uncover.

Implications for inhibitor design targeting *Ab*ATPPRT. The product formation and inhibition paths for *Ab*HisG$_S$ and *Ab*ATPPRT based on the results of this work are summarised in Scheme 2. Paths in red represent full inhibition of the respective enzyme form, while the path in yellow represents partial inhibition, with k_{cat}^{i} lower than 11.4 s^{-1}. The mechanisms of inhibition described here for known and newly discovered inhibitors may pave the way for the design of *Ab*ATPPRT inhibitors with drug-like properties. Allosteric inhibition by histidine can take place from free *Ab*ATPPRT or *Ab*ATPPRT:substrate binary complexes, in all cases likely involving a conformational change of the initial enzyme:inhibitor complex which increases the affinity of histidine for the enzyme. Depending on which substrate is evaluated, the K_i^{app} for histidine varies between 83 μM and 282 μM, which helps rationalise the dependence of *A. baumannii* on histidine biosynthesis during pneumonia. Negative feedback control by allosteric inhibition of biosynthetic enzymes evolved as a regulatory strategy to conserve cell resources, and inhibition becomes significant when the target metabolite reaches a concentration sufficient for the cell's needs.[40-41] Based on this premise, *A. baumannii* is likely

to require at least ~83 μM histidine to survive and thrive in the nutrient-deprived environment of pulmonary infection, substantially more than the ~2 μM histidine available in the lungs.[8]

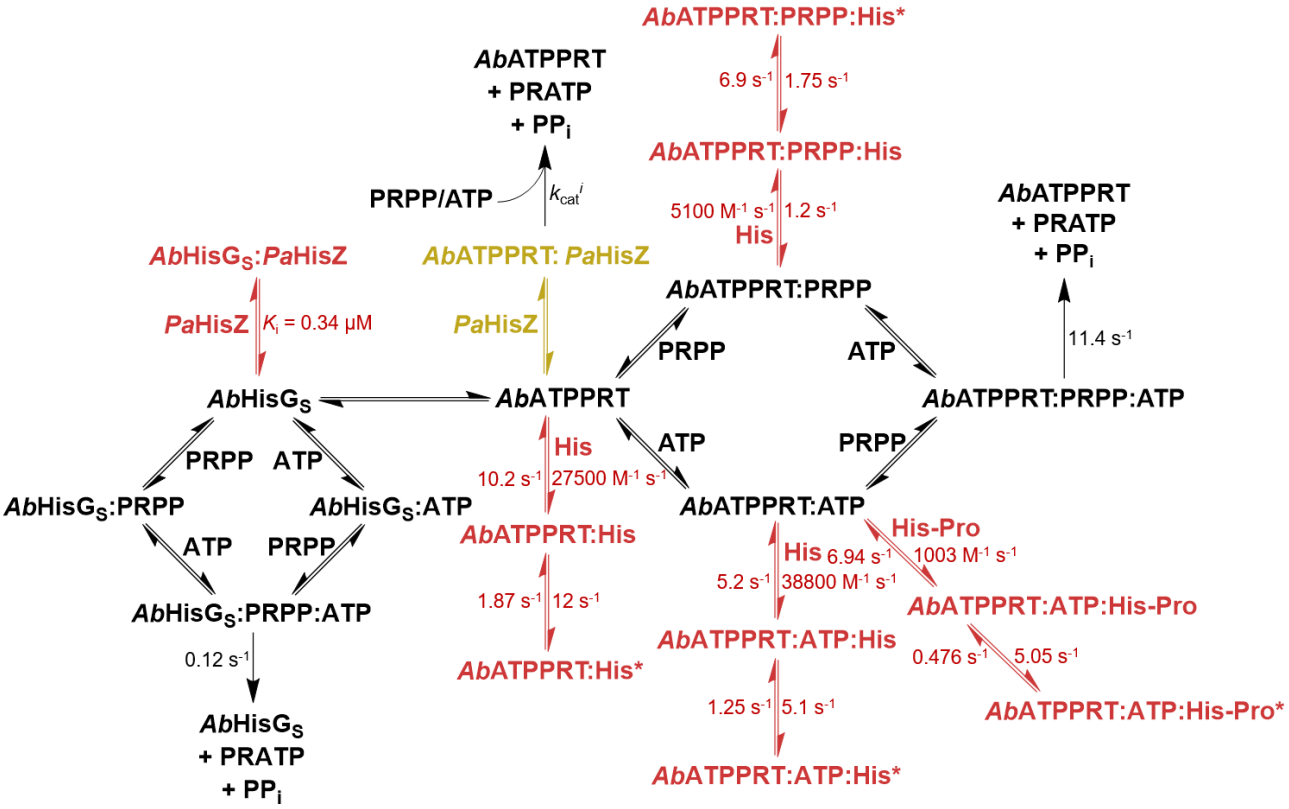

Scheme 2. Product formation and inhibition paths for *Ab*HisGs and *Ab*ATPPRT. Paths in red denote full inhibition, while the path in yellow, partial inhibition. Arrows denoting product formation encompass steps from the Michaelis complex formation up to release of the last product.

*Ab*ATPPRT follows a unique kinetic mechanism among $HisG_L$- and $HisG_S$-type ATPPRTs described to date, a rapid equilibrium random mechanism as opposed to the strictly ordered mechanisms of the other ATPPRTs.[26-28] This is an intriguing observation that will likely require structural data on *Ab*ATPPRT for a full understanding of the molecular basis underpinning this mechanism. It should be pointed out, however, orthologue-specific kinetic mechanisms are well-documented. For instance, the *Plasmodium falciparum* adenylosuccinate

synthetase follows an ordered kinetic mechanism in contrast to other orthologues which follow a random mechanism.[42]

His-Pro inhibits *Ab*ATPPRT by a mechanism distinct from histidine. Even though *Ab*HisZ is required for inhibition, and a conformational change of the initial enzyme:inhibitor complex is also likely to take place, unlike histidine the dipeptide binds only to the *Ab*ATPPRT:ATP complex with appreciable affinity, and is competitive against PRPP. Coupled with the results presented here, future structural studies to pinpoint the exact binding site of His-Pro may provide a novel route to explore rational design of drug-like inhibitors of *Ab*ATPPRT.

Finally, the surprising tight-binding inhibition of *Ab*HisG$_S$ by the HisZ orthologue from *P. arcticus* suggests that key protein:protein interactions can lead to potent allosteric inhibition of the catalytic subunit, opposite to the robust allosteric activation by protein:protein interactions with the native *Ab*HisZ. Future structural and functional mapping of the interface between *P. arcticus* HisZ and *Ab*HisG$_S$ may offer a blueprint on which to base the design of peptide mimics to recapitulate the allosteric inhibition. Antimicrobial peptides, part of the innate immunity arsenal to combat bacterial infections, and chemical analogues thereof hold potential as novel antibiotics.[43-44] Accordingly, the inhibition of *Ab*ATPPRT and *Ab*HisG$_S$ by His-Pro and *P. arcticus* HisZ, respectively, may offer new avenues for drug development targeting histidine biosynthesis to treat pneumonia caused by *A. baumannii*.

METHODS

Materials. All commercially available chemicals were used without further purification. $MgCl_2$, dithiothreitol (DTT), tricine, glycerol, lysozyme, DNase I, ampicillin, kanamycin, ATP, PRPP, POAc, L-histidine, PP_i, 3-(2-thienyl)-L-alanine (TIH), 3-(2-pyridyl)-L-alanine, 3-(3-pyridyl)-L-alanine, 3-(4-pyridyl)-L-alanine, 1-methyl-L-histidine, 3-methyl-L-

histdine, D-histidine, *β*-cyano-L-alanine, and imidazole were purchased from Merck. All other histidine analogues and histidine dipeptides (linear and cyclic) were purchased from Bachem. Ethylenediaminetetraacetic acid (EDTA)-free Cømplete protease inhibitor was purchased from Roche. Isopropyl *β*-D-1-thiogalactopyranoside (IPTG) and NaCl were purchased from Formedium. All other chemicals were purchased from readily available commercial sources. *Pa*HisG$_S$, *Pa*HisZ, *M. tuberculosis* PPase and tobacco etch virus protease (TEVP) were produced as previously described.[20]

Expression of *Ab*HisGs and *Ab*HisZ. The DNA encoding *Ab*HisG$_S$ and *Ab*HisZ (*A. baumannii* strain ATCC17978), each containing a TEVP-cleavable N-terminal His-tag with restriction sites for NdeI and HindIII at the 5′- and 3′-ends, respectively, were purchased as codon-optimised (for expression in *Escherichia coli*) gBlocks (IDT). *Ab*HisG$_S$- and *Ab*HisZ-encoding gBlocks were PCR-modified and inserted into a modified pJexpress431 and pJexpress414 plasmids, respectively, using Gibson Assembly[45] according to the manufacturer's instructions (New England Biolabs). Each construct was transformed into *E. coli* DH5α competent cells (New England Biolabs), sequenced (Eurofins) to confirm the insertion of the gene and that no mutations had been introduced, then transformed into *E. coli* BL21(DE3) competent cells (New England Biolabs). Transformed cells were grown independently in lysogeny broth (LB) containing 50 μg mL^{-1} kanamycin (for *Ab*HisG$_S$) or 100 μg mL^{-1} ampicillin (for *Ab*HisZ) at 37 °C until an optical density at 600 nm (OD_{600}) of 0.6 – 0.8, at which point cells expressing *Ab*HisG$_S$ were equilibrated to 16 °C, while those expressing *Ab*HisZ remained at 37 °C before expression was induced with 0.5 mM IPTG. Cells were grown for an additional 20 hours, harvested by centrifugation (6774 *g*, 15 mins, 4 °C) and stored at −20 °C.

Purification of *Ab*HisGs and *Ab*HisZ. Each recombinant protein was purified independently, and all purification procedures were conducted on ice or at 4 °C using an ÄTKA

Start FPLC system (GE Healthcare). All filtration of samples was by syringe through a 0.45 µm membrane. All SDS-PAGE used a NuPAGE Bis-Tris 4-12% Precast Gel (ThermoFisher Scientific) with the PageRuler Plus Stained Protein Ladder (ThermoFisher Scientific). Proteins were concentrated through a 10000 molecular weight cutoff (MWCO) ultrafiltration membrane (Millipore). Cells were thawed on ice and resuspended in Buffer A [50 mM HEPES, 500 mM NaCl, 10 mM imidazole (pH 8.0)] containing lysozyme (0.2 mg ml^{-1}), BaseMuncher (Expedeon) (0.05 mg ml^{-1}), and half a tablet of EDTA-free Cømplete protease inhibitor cocktail, disrupted in a cell disruptor (Constant systems) at 30 kpsi, and centrifuged (48000 *g*, 30 mins). The supernatant was filtered and loaded onto a HisTrap FF pre-packed column (Cytiva) pre-equilibrated with Buffer A. The column was washed with 10 column volumes (CV) of either 5% or 10% Buffer B [50 mM HEPES, 500 mM NaCl, 500 mM imidazole (pH 8.0)] for *Ab*HisZ or *Ab*HisG$_S$, respectively. *Ab*HisZ or *Ab*HisG$_S$ were eluted, respectively, with a 20-CV linear gradient of either 5-40% or 10-60% Buffer B. Fractions containing the protein of interest were pooled, mixed with TEVP at a ratio of 15 mg of target protein to 1 mg of TEVP, and dialysed against 2 × 2 L Buffer C [20 mM HEPES, 150 mM NaCl, 2 mM DTT, 10% Glycerol (pH 7.5)] over a 48-hour period, then dialysed against 2 × 2 L of Buffer A over a period of 24 hours. Samples were filtered and loaded onto a HisTrap FF Pre-packed column pre-equilibrated with Buffer A. The flow through was collected and analysed by SDS-PAGE. Each purified protein was dialysed against 2 × 2 L of their respective storage buffers: 10 mM Tris-HCl, 100 mM NaCl, 5 mM $MgCl_2$ (pH 8.0) for *Ab*HisG$_S$ and 20 mM HEPES (pH 8.0) for *Ab*HisZ. Proteins were concentrated, and their concentrations determined by UV absorbance (NanoDrop) at 280 nm using theoretical molar extinction coefficients (ε_{280}) of 43420 M^{-1} cm^{-1} (*Ab*HisZ) and 10430 (*Ab*HisG$_S$) M^{-1} cm^{-1} (ProtParam tool - Expasy). Proteins were aliquoted and stored at −80 °C. Their molecular mass was determined ESI-MS.

Oligomeric State Determination of *Ab*HisG$_S$. The oligomeric states of *Ab*HisG$_S$, *P. arcticus* HisG$_S$, *Ab*ATPPRT, and *P. arcticus* HisZ/*Ab*HisG$_S$ in solution were determined by analytical gel filtration on a Superdex 200 10/300 GL column (GE Healthcare) at 4 °C. Samples were loaded onto the column at 1 mg/mL and run in 10 mM Tris-HCl, 100 mM NaCl, 5 mM $MgCl_2$ (pH 8.0). Vitamin B12 (1350 Da), horse myoglobin (17 000 Da), chicken ovalbumin (44 000 Da), bovine γ-globulin (158 000 Da), and bovine thyroglobulin (670 000 Da) (Bio-Rad) were used as molecular weight standards. The logarithm of the molecular weight of the standards were plotted against the ratio of the elution volume (v_e) to the void volume (v_o). The data were then fitted to a linear regression, and the values of the slope and intercept were used to determine the molecular mass of each protein or protein complex.

***Ab*ATPPRT and *Ab*HisG$_S$ Activity Assays.** Unless stated otherwise, all assays were performed at 25 ºC under initial rate conditions in the forward direction in 100 mM tricine (pH 8.5), 15 mM $MgCl_2$, 100 mM KCl, 4 mM DTT, 10 μM *M. tuberculosis* PPase, 1.5 mM ATP and 1 mM PRPP, and reaction rates were measured by monitoring the increase in absorbance at 290 nm due to the formation of PRATP (ε_{290} = 3600 M^{-1} cm^{-1})[46] over 60 s with readings every 1 s in 1-cm path-length quartz cuvettes (500 μL) (Hellma) using a Shimadzu UV-2600 spectrophotometer. For *Ab*HisG$_S$ activity, the concentration of *Ab*HisG$_S$ was 2.5 μM, and for *Ab*ATPPRT activity, *Ab*HisG$_S$ and *Ab*HisZ concentrations were 0.08 μM and 2 μM, respectively ([*Ab*ATPPRT] = 0.078 μM). Reactions were incubated for 3 minutes at 25 ºC before being initiated by the addition of PRPP. Control reactions in the absence of *Ab*HisG$_S$, *Ab*HisZ, ATP, and PRPP were carried out; furthermore, controls were conducted to ensure rate was independent of *M. tuberculosis* PPase concentration. The apparent K_D for *Ab*ATPPRT was determined by measuring initial rates at 1.4 mM ATP, 1 mM PRPP, 0.04 μM *Ab*HisG$_S$, and varying *Ab*HisZ concentrations (0 – 2 μM). All steady-state kinetic measurements were made at least in duplicate.

***Ab*HisGs Substrate Saturation Curves**. *Ab*HisGs initial rates were measured at 2 mM PRPP and varying ATP concentrations (0 – 5.6 mM) for ATP saturation curves. Initial rates were measured at 5.6 mM ATP and varying PRPP concentrations (0 – 2.0 mM PRPP) for PRPP saturation curves.

Synthesis and Purification of PRATP. PRATP was synthesized as previously described.[25] Proteins were removed by passage through a 10000-MWCO Vivaspin centrifugal concentrator, and the filtrate was loaded onto a 20 mL HiTrap Q HP column (GE Healthcare) pre-equilibrated with water in a Bio-Rad NGC FPLC. The column was washed with 3 CV of water and 5 CV of 11% solution B (1 M ammonium bicarbonate). PRATP was eluted with a 20-CV linear gradient of 11 – 30% solution B. Fractions exhibiting absorbance at 290 nm were pooled, lyophilised, solubilised in 100 mM tricine pH 8.5, aliquoted and stored at −80 °C. The concentration was determined spectrophotometrically at 290 nm (ε_{290} = 3600 M^{-1} cm^{-1}). High-resolution ESI-MS and ^{31}P-NMR spectra of the purified compound were identical to those previously reported.[25].

***Ab*ATPPRT initial velocity patterns and product/dead-end inhibition.** Initial velocity patterns were determined from initial rates of *Ab*ATPPRT in the presence of varying concentrations of ATP (0.1 – 1.6 mM) and PRPP (0.1 – 1.6 mM). For product inhibition by PRATP and dead-end inhibition by POAc, *Ab*ATPPRT activity was monitored at several fixed concentrations of each product: either PRATP (0 – 100 μM) or POAc (0 – 10 mM). Measurements were conducted at two distinct fixed concentrations of one substrate (low and high) whilst varying the concentration of the other. For each fixed concentration of either ATP (0.15 mM and 1.6 mM) or PRPP (0.2 mM and 1.6 mM), the concentration of the co-substrate was varied from 0.1 mM to 1.6 mM.

***Ab*ATPPRT reaction in the reverse direction.** Initial rates of *Ab*ATPPRT (0.078 μM) in the reverse direction were measured at 25 °C. Reactions (500 μL) contained 100 mM tricine (pH 8.5) 15 mM $MgCl_2$, 100 mM KCl, and 4 mM DTT. Reaction rates were measured by monitoring the decrease in absorbance at 290 nm due to the consumption of PRATP (60 μM) in 1-cm path-length quartz cuvettes (Hellma) using a Shimadzu UV-2600 spectrophotometer. Rates were measured in the presence of either 2 mM PP_i or 4 mM POAc, and a control in the absence of both PP_i and POAc.

***Ab*ATPPRT activity in the presence of L-histidine Analogues and L-histidine-containing dipeptides.** Initial rates of *Ab*ATPPRT in the presence of 12 different L-histidine analogues (2 mM) and 14 commercially available L-histidine-containing linear dipeptides (1 mM, except His-Trp at 0.25 mM) were measured. Dose-response curves for 3-(4-pyridyl)-L-alanine, 1-methyl-L-histidine, and D-histidine were determined by measuring *Ab*ATPPRT initial rates in the presence of varying concentrations of the respective histidine analogue (0 – 8 mM), and for cyclo-di-His-Pro, in the presence of varying concentrations of cyclo-di-His-Pro (0 – 4 mM). ATP concentration was 0.16 mM and PRPP concentration was 0.21 mM.

***Ab*ATPPRT inhibition by histidine, His-Pro and His-Trp against *Ab*ATPPRT.** The dose-response curve for histidine was determined from initial rates of *Ab*ATPPRT in the presence of 0 – 640 μM histidine, 1.4 mM ATP and 1 mM PRPP, either in the presence or absence of 2 μM *P. arcticus* HisZ. The dose-response curve for His-Pro was determined from initial rates of *Ab*ATPPRT in the presence of 0 – 8 mM His-Pro, 0.16 mM ATP and 0.21 mM PRPP. Alternatively, initial rates of *Ab*$HisG_S$ were determined in the presence of 0 – 8 mM His-Pro, 0.63 mM ATP and 0.60 mM PRPP. The dose-response curve for His-Trp was determined from initial rates in the presence of 0 – 0.4 mM His-Trp in an Applied Photophysics SX-20 stopped-flow spectrophotometer outfitted with a 5-μL mixing cell (0.5-cm path length and 0.9-ms dead time) and a circulating water bath. The steady-state mechanism of inhibition

by histidine and His-Pro were investigated by measuring the initial rates of *Ab*ATPPRT at saturating concentration of one substrate (1.6 mM) and varying concentrations of the co-substrate (0.1 – 1.6 mM) in the presence of different fixed concentrations of either histidine (0 – 400 μM) or His-Pro (0 – 6 mM). Whether or not His-Pro led to dissociation of the *Ab*ATPPRT hetero-octamer was probed from initial rates of *Ab*HisG$_S$ (6 μM) in the presence or absence of 10 mM His-Pro and from initial rates of *Ab*ATPPRT (6 μM) in the presence of 10 mM His-Pro, with 6.4 mM ATP and 0.21 mM PRPP. To test for slow-onset inhibition of His-Pro, the rate of PRATP formation by *Ab*ATPPRT (16 nM) was measured for 20 min in the presence of 3.2 mM ATP, 4.2 mM PRPP, and 0 – 8 mM His-Pro, with reactions initiated by the addition of enzyme.

DSF of *Ab*HisG$_S$, *Ab*HisZ, and *Ab*ATPPRT. DSF measurements (λ_{ex} = 490 nm; λ_{em} = 610 nm) were performed in a 96-well plate (50 μL) on a Stragene Mx3005p instrument. Thermal denaturation of *Ab*HisG$_S$ (7.5 μM) was measured in the presence of either substrate (either 0 – 8 mM ATP or 0 – 8 mM PRPP), product (either 0.5 mM PRATP or 1.0 mM PP_i) or His-Pro (8 mM). Thermal denaturation of *Ab*HisZ (9 μM) was measured in the presence of 0 – 1 mM histidine. Thermal denaturation of *Ab*ATPPRT (7 μM, achieved by mixing 7.5 μM of *Ab*HisG$_S$ and 7.5 μM of *Ab*HisZ) was measured in the absence and presence of products (either 0.5 mM PRATP or 1.0 mM PP_i). Assays were conducted in 100 mM tricine (pH 8.5), 100 mM KCl, 4 mM DTT, and 15 mM $MgCl_2$. Sypro Orange (5X) (Invitrogen) was added to all wells. Thermal denaturation curves were recorded in triplicate over a range of 25 – 90 °C with 1-°C min^{-1} increments. Controls lacking protein were subtracted from curves with the respective protein.

Binding kinetics of histidine and His-Pro to *Ab*ATPPRT. Rapid kinetics of histidine and His-Pro binding to *Ab*ATPPRT were carried out by monitoring the change in internal tryptophan fluorescence (λ_{ex} = 290 nm; λ_{em} > 320 nm) at 25 °C in an Applied Photophysics SX-

20 stopped-flow spectrofluorimeter outfitted with a 5-μL mixing cell (0.5-cm path length and 0.9-ms dead time) and a circulating water bath. In all experiments, each syringe contained 100 mM tricine (pH 8.5), 15 mM $MgCl_2$, 100 mM KCl, and 4 mM DTT. *Ab*ATPPRT (2.5 μM; 2.8 μM *Ab*HisG$_S$ and 2.8 μM *Ab*HisZ) (in the presence or absence of either 1.6 mM ATP or 2.1 mM PRPP) binding to either histidine (0 – 1280 μM) or His-Pro (0.5-8 mM) was measured by rapidly mixing 55 μL from each syringe, and fluorescence change was monitored for up to 5 s with 8 traces averaged for each concentration and 5000 datapoints collected per trace. Controls lacked ligand. Absorbances at 290 nm and 1-cm path length of 1280 μM histidine and 8 mM His-Pro were lower than 0.01, indicating no inner filter effect interfered with the fluorescence measurements.

Inhibition of *Ab*HisG$_S$ and *Ab*ATPPRT by *P. arcticus* HisZ. Initial rates of *Ab*HisG$_S$ (1 μM) at 4.8 mM ATP and 2 mM PRPP were measured in the presence of 0 – 8 μM *P. arcticus* HisZ either in the presence or absence of 600 μM histidine. Initial rates of *Ab*ATPPRT (0.154 μM) at 1.4 mM ATP and 1 mM PRPP were measured in the presence of 0 – 2 μM *P. arcticus* HisZ. Initial rates of *Ab*HisG$_S$ (0.16 μM) at 1.4 mM ATP, 1 mM PRPP, and 2 μM *Pa*HisZ were measured in the presence of 0 – 2 μM *Ab*HisZ. Initial rates of *Ab*HisG$_S$ (0.609 μM) at 4.8 mM ATP and 2 mM PRPP were measured in the presence and absence of 4 μM BSA.

Kinetics and thermal denaturation data analysis. Kinetic and thermal denaturation data were analysed by the non-linear regression function of SigmaPlot 14.0 (SPSS Inc.). Data points and error bars represent mean ± SEM, and kinetic and equilibrium constants are given as mean ± fitting error. Substrate saturation curves at a fixed concentration of the co-substrate were fitted to eq 1. Initial rate data at varying concentrations of *Ab*HisZ were fitted to eq 2, and the concentration of *Ab*ATPPRT at any concentration of *Ab*HisG$_S$ and *Ab*HisZ was calculated according to eq 3. Initial velocity patterns were globally fitted to eq 4. Competitive inhibition data were fitted to eq 5, and noncompetitive, to eq 6. Dose-response curves for histidine and

His-Pro were fitted to eq 7. The overall equilibrium dissociation constant was calculated with eq 8. Uncompetitive inhibition data were fitted to eq 9. Dose-response curve for *P. arcticus* HisZ was fitted to eq 10. Thermal denaturation curves were fitted to eq 11.[47] In eqs 1 – 11, v is the initial rate, k_{cat} is the steady-state turnover number, K_M is the apparent Michaelis constant, E_T is total enzyme concentration, S is the concentration of the varying substrate when the co-substrate is held constant, V_{max} is the maximal velocity, G is the concentration of *Ab*HisG$_S$, Z is the concentration of *Ab*HisZ, K_D^{app} is the apparent equilibrium dissociation constant, and *AbATPPRT* is the concentration of *Ab*HisG$_S$-*Ab*HisZ complex, A and B are the concentrations of varying substrates and K_a and K_b are their respective Michaelis constants, K_{ia} is the apparent dissociation constant for the complex between enzyme and substrate A when the concentration of B approaches zero, I is the concentration of inhibitor, K_{is} and K_{ii} are respectively the slope and intercept inhibition constants, v_i and v_0 are the initial rate in the presence and absence of inhibitor, respectively, IC_{50} is the half-maximal inhibitory concentration, h is the Hill coefficient, K_D is the equilibrium dissociation constant, $k_1 – k_4$ are rate constants governing elementary steps for the two-step binding mechanism with isomerisation of the initial EI complex denoted in Scheme S2, K_i^{app} is the apparent dissociation constant, F_U is fraction unfolded, T is the temperature in °C, T_m is the melting temperature, c is the slope of the transition region, and *LL* and *UL* are folded and unfolded baselines, respectively.

$$\frac{v}{E_T} = \frac{k_{cat}S}{K_M+S} \qquad \text{eq 1}$$

$$v = V_{max}\frac{G+Z+K_D^{app}-\sqrt{(G+Z+K_D^{app})^2-4GZ}}{2G} \qquad \text{eq 2}$$

$$AbATPPRT = \frac{(G+Z+K_D)-\sqrt{(G+Z+K_D)^2-4GZ}}{2} \qquad \text{eq 3}$$

$$\frac{v}{E_T} = \frac{k_{cat}AB}{K_{ia}K_b+K_aB+K_bA+AB} \qquad \text{eq 4}$$

$$\frac{v}{E_T} = \frac{k_{cat}S}{\left(1+\frac{I}{K_{is}}\right)K_M+S} \quad \text{eq 5}$$

$$\frac{v}{E_T} = \frac{k_{cat}S}{\left(1+\frac{I}{K_{is}}\right)K_M+\left(1+\frac{I}{K_{ii}}\right)S} \quad \text{eq 6}$$

$$\frac{v_i}{v_0} = \frac{1}{1+\left(\frac{I}{IC_{50}}\right)^h} \quad \text{eq 7}$$

$$K_D = \frac{k_2\, k_4}{k_1(k_3+k_4)} \quad \text{eq 8}$$

$$\frac{v}{E_T} = \frac{k_{cat}S}{K_M+\left(1+\frac{I}{K_{ii}}\right)S} \quad \text{eq 9}$$

$$\frac{v_i}{v_0} = 1 - \frac{(E_T+I+K_i^{app})-\sqrt{\left(E_T+I+K_i^{app}\right)^2-4E_TI}}{2E_T} \quad \text{eq 10}$$

$$F_U = LL + \frac{UL-LL}{1+e^{(Tm-T)/c}} \quad \text{eq 11}$$

SUPPORTING INFORMATION

Further experimental and computational characterisation of *Ab*ATPPRT kinetics, inhibition, oligomeric state and thermal denaturation; substrate and inhibitor binding kinetic schemes; chemical structures of histidine analogues and histidine-containing dipeptides; amino acid sequence alignments; equation derivation.

CORRESPONDING AUTHOR

Rafael G. da Silva - School of Biology, Biomedical Sciences Research Complex, University of St Andrews, St Andrews, Fife KY16 9ST, United Kingdom; Email: rgds@st-andrews.ac.uk, phone: +44 (0)1334 463496.

ACKNOWLEDGEMENTS

This work was supported by the Biotechnology and Biological Sciences Research Council (BBSRC) (Grant BB/M010996/1) via EASTBIO Doctoral Training Partnership studentships

to B. J. R. and G. F., and by the Engineering and Physical Sciences Research Council (EPSRC) [grant number EP/L016419/1] via a CRITICAT Centre for Doctoral Training studentship to T.F.G.M. The authors are grateful to the BSRC Mass Spectrometry and Proteomics Facility for the ESI-MS analysis of *Ab*HisG$_S$ and *Ab*HisZ. In memory of Dr John S. Blanchard.

ABREVIATIONS

ATPPRT, ATP phosphoribosyltransferase; PRPP, 5-phospho-α-D-ribosyl-1-pyrophosphate; PRATP, N^1-(5-phospho-β-D-ribosyl)-ATP; PP_i, inorganic pyrophosphate; DTT, dithiothreitol; DSF, differential scanning fluorimetry; *Ab*ATPPRT, *A. baumannii*, ATPPRT; *Ab*HisG$_S$, *A. baumannii*, HisG$_S$; *Ab*HisZ, *A. baumannii*, HisZ; PPase, pyrophosphatase; MWCO, molecular weight cut off; ESI-MS, electrospray ionisation mass spectrometry; His-Pro, L-histidine-L-proline.

REFERENCES

(1) Tacconelli, E., Carrara, E., Savoldi, A., Harbarth, S., Mendelson, M., Monnet, D. L., Pulcini, C., Kahlmeter, G., Kluytmans, J., Carmeli, Y., Ouellette, M., Outterson, K., Patel, J., Cavaleri, M., Cox, E. M., Houchens, C. R., Grayson, M. L., Hansen, P., Singh, N., Theuretzbacher, U., and Magrini, N. Discovery, research, and development of new antibiotics: the WHO priority list of antibiotic-resistant bacteria and tuberculosis. *Lancet Infect. Dis.* 2018, 18, 318-327.

(2) Magill, S. S., Edwards, J. R., Bamberg, W., Beldavs, Z. G., Dumyati, G., Kainer, M. A., Lynfield, R., Maloney, M., McAllister-Hollod, L., Nadle, J., Ray, S. M., Thompson, D. L., Wilson, L. E., and Fridkin, S. K. Multistate point-prevalence survey of health care-associated infections. *N. Engl. J. Med.* 2014, 370, 1198-1208.

(3) Ma, C., and McClean, S. Mapping global prevalence of *Acinetobacter baumannii* and recent vaccine development to tackle it. *Vaccines* 2021, 9, 570.

(4) Giammanco, A., Calà, C., Fasciana, T., and Dowzicky, M. J. Global assessment of the activity of tigecycline against multidrug-resistant gram-negative pathogens between 2004 and 2014 as part of the tigecycline evaluation and surveillance trial. *mSphere* 2017, 2, e00310-16.

(5) Harding, C. M., Hennon, S. W., and Feldman, M. F. Uncovering the mechanisms of *Acinetobacter baumannii* virulence. *Nat. Rev. Microbiol.* 2018, 16, 91-102.

(6) Spellberg, B., and Rex, J. H. The value of single-pathogen antibacterial agents. *Nat. Rev. Drug Disc.* 2013, 12, 963.

(7) Martínez-Guitián, M., Vázquez-Ucha, J. C., Álvarez-Fraga, L., Conde-Pérez, K., Lasarte-Monterrubio, C., Vallejo, J. A., Bou, G., Poza, M., and Beceiro, A. Involvement of hisf in the persistence of *Acinetobacter baumannii* during a pneumonia infection. *Front. Cell. Infect. Microbiol.* 2019, 9, 310.

(8) Lonergan, Z. R., Palmer, L. D., and Skaar, E. P. Histidine utilization is a critical determinant of *Acinetobacter* pathogenesis. *Infect. Immun.* 2020, 88, e00118-20.

(9) Holdgate, G. A., Meek, T. D., and Grimley, R. L. Mechanistic enzymology in drug discovery: a fresh perspective. *Nat. Rev. Drug Disc.* 2018, 17, 115-132.

(10) Cabral, M. P., Soares, N. C., Aranda, J., Parreira, J. R., Rumbo, C., Poza, M., Valle, J., Calamia, V., Lasa, I., and Bou, G. Proteomic and functional analyses reveal a unique lifestyle for *Acinetobacter baumannii* biofilms and a key role for histidine metabolism. *J. Proteome Res.* 2011, 10, 3399-3417.

(11) Nairn, B. L., Lonergan, Z. R., Wang, J., Braymer, J. J., Zhang, Y., Calcutt, M. W., Lisher, J. P., Gilston, B. A., Chazin, W. J., de Crécy-Lagard, V., Giedroc, D. P., and Skaar, E. P. The Response of Acinetobacter baumannii to Zinc Starvation. *Cell Host Microbe* 2016, 19, 826-836.

(12) Wang, N., Ozer, E. A., Mandel, M. J., and Hauser, A. R. Genome-wide identification of *Acinetobacter baumannii* genes necessary for persistence in the lung. *mBio* 2014, 5, e01163-14.

(13) Bell, R. M., and Koshland, D. E. Allosteric properties of the first enzyme of the histidine operon. *Bioorg. Chem.* 1971, 1, 409-423.

(14) Ames, B. N., Martin, R. G., and Garry, B. J. (1961) The first step of histidine biosynthesis. *J. Biol. Chem.* 236, 2019-2026.

(15) Martin, R. G. The first enzyme in histidine biosynthesis: the nature of feedback inhibition by histidine. *J. Biol. Chem.* 1963, 238, 257-268.

(16) Mittelstadt, G., Moggre, G. J., Panjikar, S., Nazmi, A. R., and Parker, E. J. *Campylobacter jejuni* adenosine triphosphate phosphoribosyltransferase is an active hexamer that is allosterically controlled by the twisting of a regulatory tail. *Protein Sci.* 2016, 25, 1492-1506.

(17) Pisco, J. P., de Chiara, C., Pacholarz, K. J., Garza-Garcia, A., Ogrodowicz, R. W., Walker, P. A., Barran, P. E., Smerdon, S. J., and de Carvalho, L. P. S. Uncoupling conformational states from activity in an allosteric enzyme. *Nat. Commun.* 2017, 8, 203.

(18) Sissler, M., Delorme, C., Bond, J., Ehrlich, S. D., Renault, P., and Francklyn, C. An aminoacyl-tRNA synthetase paralog with a catalytic role in histidine biosynthesis. *Proc. Natl. Acad. Sci. USA* 1999, 96, 8985-8990.

(19) Livingstone, E. K., Mittelstadt, G., Given, F. M., and Parker, E. J. Independent catalysis of the short form HisG from *Lactococcus lactis*. *FEBS Lett.* 2016, 590, 2603-2610.

(20) Stroek, R., Ge, Y., Talbot, P. D., Glok, M. K., Bernas, K. E., Thomson, C. M., Gould, E. R., Alphey, M. S., Liu, H., Florence, G. J., Naismith, J. H., and da Silva, R. G. Kinetics and structure of a cold-adapted hetero-octameric ATP phosphoribosyltransferase. *Biochemistry* 2017, 56, 793-803.

(21) Bovee, M. L., Champagne, K. S., Demeler, B., and Francklyn, C. S. The quaternary structure of the HisZ-HisG N-1-(5'-phosphoribosyl)-ATP transferase from *Lactococcus lactis*. *Biochemistry* 2002, 41, 11838-11846.

(22) Vega, M. C., Zou, P., Fernandez, F. J., Murphy, G. E., Sterner, R., Popov, A., and Wilmanns, M. Regulation of the hetero-octameric ATP phosphoribosyl transferase complex from *Thermotoga maritima* by a tRNA synthetase-like subunit. *Mol. Microbiol.* 2005, 55, 675-686.

(23) Champagne, K. S., Sissler, M., Larrabee, Y., Doublie, S., and Francklyn, C. S. Activation of the hetero-octameric ATP phosphoribosyl transferase through subunit interface rearrangement by a tRNA synthetase paralog. *J. Biol. Chem.* 2005, 280, 34096-34104.

(24) Thomson, C. M., Alphey, M. S., Fisher, G., and da Silva, R. G. Mapping the structural path for allosteric inhibition of a short-form ATP phosphoribosyltransferase by histidine. *Biochemistry* 2019, 58, 3078-3086.

(25) Alphey, M. S., Fisher, G., Ge, Y., Gould, E. R., Machado, T. G., Liu, H., Florence, G. J., Naismith, J. H., and da Silva, R. G. Catalytic and anticatalytic snapshots of a short-form ATP phosphoribosyltransferase. *ACS Catal.* 2018, 8, 5601–5610.

(26) Fisher, G., Thomson, C. M., Stroek, R., Czekster, C. M., Hirschi, J. S., and da Silva, R. G. Allosteric activation shifts the rate-limiting step in a short-form ATP phosphoribosyltransferase. *Biochemistry* 2018, 57, 4357-4367.

(27) Morton, D. P., and Parsons, S. M. Biosynthetic direction substrate kinetics and product inhibition studies on the first enzyme of histidine biosynthesis, adenosine triphosphate phosphoribosyltransferase. *Arch. Biochem. Biophys.* 1976, 175, 677-686.

(28) Mittelstadt, G., Jiao, W., Livingstone, E. K., Moggre, G. J., Nazmi, A. R., and Parker, E. J. A dimeric catalytic core relates the short and long forms of ATP-phosphoribosyltransferase. *Biochem. J.* 2018, 475, 247-260.

(29) Bartee, D., and Freel Meyers, C. L. Targeting the unique mechanism of bacterial 1-deoxy-D-xylulose-5-phosphate synthase. *Biochemistry* 2018, 57, 4349-4356.

(30) Cleland, W. W. The kinetics of enzyme-catalyzed reactions with two or more substrates or products. III. Prediction of initial velocity and inhibition patterns by inspection. *Biochim. Biophys. Acta* 1963, 67, 188-196.

(31) Segel, I. H., (1975) *Enzyme kinetics. Behavior and analysis of rapid equilibrium and steady-state systems*. 1st ed.; Wiley & Sons, Inc.: New York, NY.

(32) Moggre, G. J., Poulin, M. B., Tyler, P. C., Schramm, V. L., and Parker, E. J. Transition state analysis of adenosine triphosphate phosphoribosyltransferase. *ACS Chem. Biol.* 2017, 12, 2662-2670.

(33) Pedreno, S., Pisco, J. P., Larrouy-Maumus, G., Kelly, G., and de Carvalho, L. P. Mechanism of feedback allosteric inhibition of ATP phosphoribosyltransferase. *Biochemistry* 2012, 51, 8027-8038.

(34) Champagne, K. S., Piscitelli, E., and Francklyn, C. S. Substrate recognition by the hetero-octameric ATP phosphoribosyltransferase from *Lactococcus lactis*. *Biochemistry* 2006, 45, 14933-14943.

(35) Johnson, K. A. Fitting enzyme kinetic data with KinTek Global Kinetic Explorer. *Methods Enzymol.* 2009, 467, 601-626.

(36) Johnson, K. A., Simpson, Z. B., and Blom, T. FitSpace explorer: an algorithm to evaluate multidimensional parameter space in fitting kinetic data. *Anal. Biochem.* 2009, 387, 30-41.

(37) Koshland, D. E., Jr., Némethy, G., and Filmer, D. Comparison of experimental binding data and theoretical models in proteins containing subunits. *Biochemistry* 1966, 5, 365-385.

(38) Fersht, A., (1999) *Structure and mechanism in protein science*. 1st ed.; W. H. Freeman and Company: New York, NY.

(39) Vogt, A. D., and Di Cera, E. Conformational selection or induced fit? A critical appraisal of the kinetic mechanism. *Biochemistry* 2012, 51, 5894-5902.

(40) Gerhart, J. C., and Pardee, A. B. The enzymology of control by feedback inhibition. *J. Biol. Chem.* 1962, 237, 891-896.

(41) Monod, J., Changeux, J.-P., and Jacob, F. Allosteric proteins and cellular control systems. *J. Mol. Biol.* 1963, 6, 306-329.

(42) Raman, J., Mehrotra, S., Anand, R. P., and Balaram, H. Unique kinetic mechanism of *Plasmodium falciparum* adenylosuccinate synthetase. *Mol. Biochem. Parasitol.* 2004, 138, 1-8.

(43) Li, W., Tailhades, J., O'Brien-Simpson, N. M., Separovic, F., Otvos, L., Jr., Hossain, M. A., and Wade, J. D. Proline-rich antimicrobial peptides: potential therapeutics against antibiotic-resistant bacteria. *Amino Acids* 2014, 46, 2287-2294.

(44) Li, W., Separovic, F., O'Brien-Simpson, N. M., and Wade, J. D. Chemically modified and conjugated antimicrobial peptides against superbugs. *Chem. Soc. Rev.* 2021, 50, 4932-4973.

(45) Gibson, D. G. Synthesis of DNA fragments in yeast by one-step assembly of overlapping oligonucleotides. *Nucleic Acids Res.* 2009, 37, 6984-6990.

(46) Smith, D. W., and Ames, B. N. Phosphoribosyladenosine monophosphate, an intermediate in histidine biosynthesis. *J. Biol. Chem.* 1965, 240, 3056-3063.

(47) Niesen, F. H., Berglund, H., and Vedadi, M. The use of differential scanning fluorimetry to detect ligand interactions that promote protein stability. *Nat. Protoc.* 2007, 2, 2212-21.

“For Table of Contents Use Only”

Allosteric inhibition of *Acinetobacter baumannii* ATP phosphoribosyltransferase by protein:dipeptide and protein:protein interactions

Benjamin J. Read, Gemma Fisher, Oliver L. R. Wissett, Teresa F. G. Machado, John Nicholson, John B. O. Mitchell, and Rafael G. da Silva

A. baumannii ATP phosphoribosyltransferase follows a rapid equilibrium random kinetic mechanism, depicted in Cleland’s notation. The activated enzyme is inhibited by histidine and His-Pro, while the non-activated enzyme is inhibited by *P. arcticus* HisZ.